**EUROPEAN ORGANIZATION FOR NUCLEAR RESEARCH**
**European Laboratory for Particle Physics**
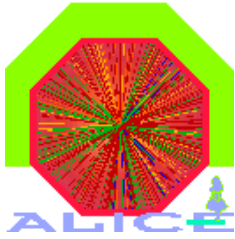
# Straggling functions and PID capabilities of the ALICE TPC

**Authors:**

P. Christiansen, J. Baechler
for the ALICE TPC Collaboration

**Abstract:**

An Inner Readout Chamber (IROC) of the ALICE TPC was tested at the CERN PS T10 beam line. For protons with momentum $p = 1$ and $3$ GeV/c the straggling function and specific energy loss distribution was extracted and compared to model calculations by Hans Bichsel. Good agreement was found when detector effects were taken into account. Unfortunately these effects increase the resolution of the energy loss measurement and correlate measurements in neighboring rows. For a MIP the resolution increases from 7.9 % to 9.3 % for the test beam data.

For the full ALICE TPC the resolution is estimated to be 4.9 % for a MIP after 2.5 m drift. The resolution is better than the 5.5 % quoted in the TDR and allows a $4\sigma$ separation of pions and protons for $3 \leq p_T \leq 20$ GeV/c.

# Contents

# 1 Introduction

The ALICE TPC [1] will, in addition to tracking, provide particle identification (PID) based on the energy loss information. In this note the data from the TPC prototype test is used to study the PID performance. Two different approaches to PID is used:

- **Truncated mean C**: For each track the truncated mean $C$ is constructed by taking the mean of the 60% lowest cluster[1] charge values. The estimator $C$ is called the specific energy loss and is approximately Gaussian distributed which make it the standard TPC PID method. The quoted (energy loss) resolution is the relative with of this Gaussian.

- **The straggling function**: For a given track segment (e.g. the track length over a pad) the cluster charge probability density distribution is called the cluster charge straggling function. The straggling function is related to the underlying energy loss mechanism, and it can be used to fit the cluster charge distribution in a single track to take into account the full information.

Using the specific energy loss measured by the TPC it is possible to do track by track PID of $\pi, K, p,$ and $e$ in part of the low transverse momentum range $p_T \leq 1$ GeV/c, with an energy loss resolution less than 10% [3]. Recently the STAR experiment at RHIC have demonstrated that statistical PID is also feasible on the relativistic rise ($\beta\gamma > 4$, $p_T > 2$ GeV/c) with a resolution of 8%. Figure 1 shows the measurement of the $\bar{p}/\pi$ ratio as a functions of transverse momentum for particles identified with the RICH and the TPC. Note that this analysis is statistics limited at high $p_T$ and has recently been

---

[1]In the following, the word cluster is associated with the reconstructed hit in a pad row in the TPC and not the use of Blum and Rolandi ( [2], page 15), where cluster-size is used for the total number of electrons generated in a single scattering.
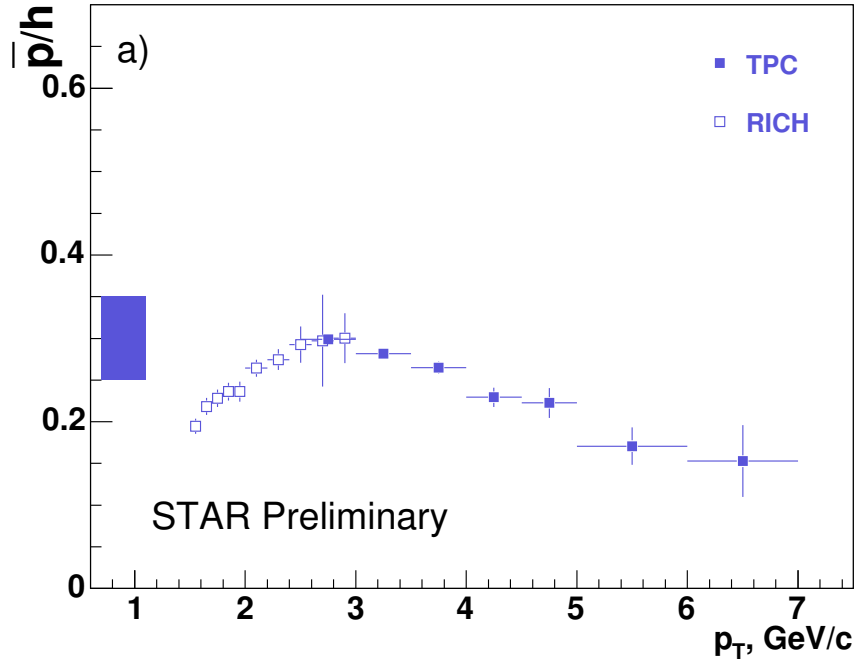
Figure 1: $\bar{p}/\pi$ ratio measured by STAR. The solid points are extracted using the PID capabilities of the STAR TPC. Figure is taken from [4].

extended to $p_T \sim 10$ GeV/c [5]. There is also a new paper on combined TOF and TPC PID by STAR [6] where the focus is on the intermediate to high-$p_T$ region and results are compared with calculations by Hans Bichsel.

In principle statistically PID of $\pi, K$, and $p$ can be done up to 50 GeV/c or more. This is because the average energy loss has an almost constant separation for different particle species in this transverse momentum interval (the energy loss rises logarithmically from $\beta\gamma \sim 3.6$ (MIP) to $\beta\gamma \sim 1000$ (the plateau), see Figure 17). This is not the case for the velocity difference which is the PID principle of Cherenkov and TOF.

Results at RHIC have shown the importance of high $p_T$ physics so it is a high priority for ALICE to exploit the detector capabilities to a maximum. In this note the energy loss measurements done with the TPC will be studied in detail for protons with momentum $p = 1$ and 3 GeV/c and compared to model calculations by Hans Bichsel. Based on the understanding extracted from this comparison the PID separation capabilities of the full ALICE TPC is evaluated.

The data used here were collected with the test TPC at the T10 beam line with a mono energetic beam. The setup and results on gain homogeneity and energy loss resolution of the truncated mean have already been described in an ALICE note [7].

Here we shall first give a short introduction to the theoretical calculations by Hans Bichsel of the straggling functions and their characteristics (section 2). Then the experimental measurements will be described (section 3) and compared to the theoretical (section 4)). Finally the consequences for the full ALICE TPC are computed (section 5).
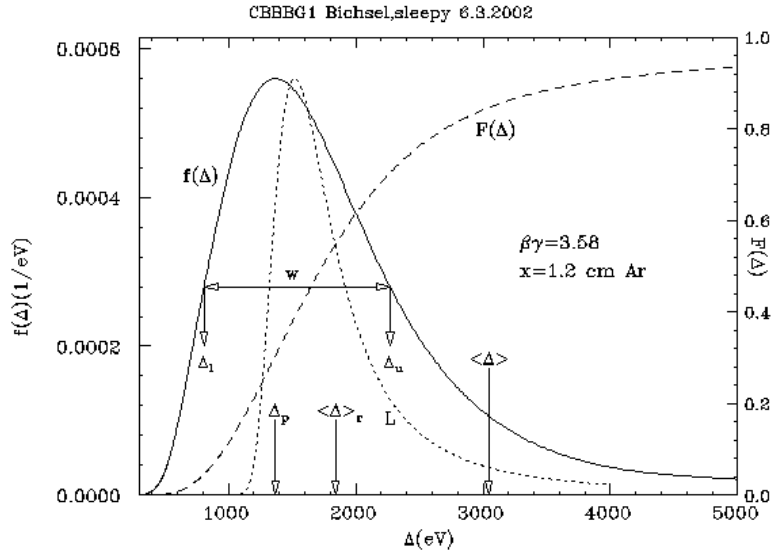
3

# 2 Hans Bichsel's calculations



Figure 2: The calculated straggling function, $f(\Delta)$, for a MIP traversing 1.2 cm of Ar is shown by the solid line. As can be seen there is a big difference between the most probably energy loss, $\Delta_p$, and the mean energy loss, $\langle\Delta\rangle$ (which is the $dE/dx$ obtained with the Bethe-Bloch formula). The Landau function is given by the dotted line and is significantly narrower because the number of primary collisions is much larger (also no atomic structure effects are taken into account). Figure is taken from [8].

The calculations and results of Hans Bichsel are described in detail in [8] which should soon be published. Here only the main features of the calculations will be described.

The energy loss straggling function $f(\Delta)$ describes the probability for a particle with a given $\beta\gamma$ to loose the energy, $\Delta$, when traversing the length $x$ of a specified material. An example of a straggling function (or Landau distribution) is shown in Figure 2.

The simplest approach to the calculation of the energy loss is to use the Rutherford cross section, $\sigma_R(E)$, which describes the energy loss, $E$, of a charged particle with speed $\beta$ interacting with an electron at rest:

$$\sigma_R(E) = \frac{k}{\beta^2} \frac{(1 - \beta^2 E/E_{\max})}{E^2}. \tag{1}$$

Note that the cross section does not depend on the mass of the particle and that for a fixed $\beta$ and $E \ll E_{\max}$, $\sigma_R(E) \propto 1/E^2$.

To take into account that the electrons are bound in matter an atomic model is used. The model used by Bichsel is the Fermi-virtual-photon (FVP) model also known as the Photo-Absorption-Ionization model. In this model the cross section, $\sigma(E; \beta\gamma)$, only depends on
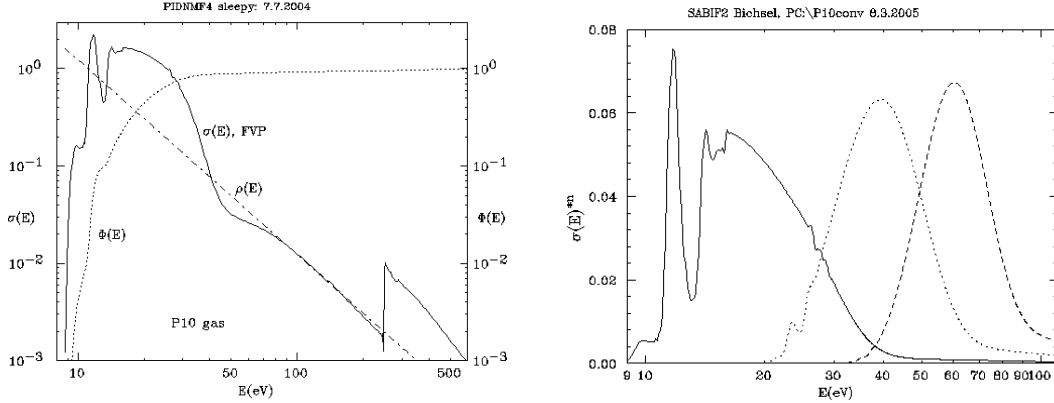
4

Figure 3: Left: The cross section $\sigma(E)$ for a MIP in P10. Right: The energy loss $E$ for 1, 2, and 3 collisions. The atomic structure is no longer visible after only a few collisions, but remain important for the FWHM. Figure is taken from [8].

the dipole-oscillator-strength (DOS) which can be extracted from optical measurements. The calculated cross section $\sigma(E)$ for a MIP in Ar is shown in Figure 3 (left).
The single collisions cross section $\sigma_t(\beta\gamma)$ is:

$$\sigma_t(\beta\gamma) = \int_0^{E_{\max}} \sigma(E;\beta\gamma)dE, \tag{2}$$

The probability density function (pdf) for the energy loss $E$ (in a single collision) is then $P(E) = \sigma(E)/\sigma_t$.
The total energy loss in several collisions is $\Delta = \sum_i E_i$. Given the number of collisions $n$ the pdf for $\Delta$ is:

$$P_n(\Delta) = \int_0^{\Delta} P(E) \cdot P_{n-1}(\Delta - E)dE \tag{3}$$

The mean free path, $\lambda$, is:

$$\lambda = \frac{1}{N\sigma_t(\beta\gamma)}, \tag{4}$$

where N is the number of atoms per unit volume. The number of collisions in a segment with length $x$ is Poisson distributed with mean, $\mu = x/\lambda$. The energy loss straggling function (pdf), $f(\Delta)$, can then be calculated as:

$$f(\Delta) = \sum_{n=0}^{\infty} \frac{\mu^n e^{-\mu}}{n!} P_n(\Delta;\beta\gamma), \tag{5}$$

The actual calculations is done by a numerical folding of the distributions according to equation 5 for a short segment length $x'$. The final straggling function for a segment length

$x = i \cdot x'$ (where $i$ is an integer) is then found by folding $i$ times the straggling function for $x'$. This method gives the same accuracy as a high statistics Monte Carlo simulation but is much faster. Description of this method and other methods for calculating the straggling function can be found in [9] (sections VI and VII).

With the TPC it is impossible to measure the energy loss, instead the charge $Q$ collected on the pads is measured. To take this into account in the model a simple simulation is performed, see section 4. More information about this can be found in Bichsel's paper.

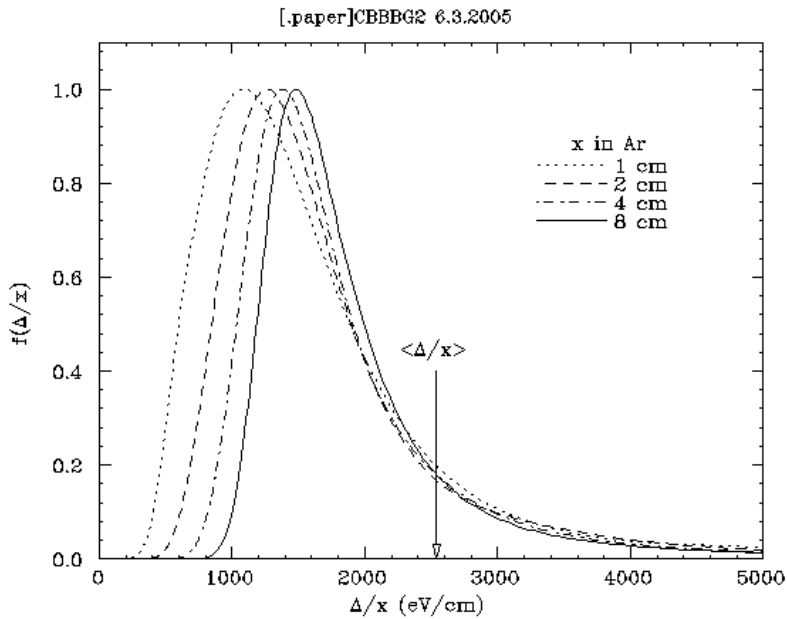## 2.1  Scaling of the straggling functions

Figure 4: Calculated straggling functions for a MIP in Ar normalized to the segment length ($x$). The mean energy loss per length is the same while the most likely value increases with the length of the segments (pads). Figure is taken from [8].

Figure 4 shows the MIP straggling functions in Ar for different pad geometries. It is observed in the paper by Bichsel that it is not possible to relate the different straggling functions by a single parameter scaling, e.g., by adjusting the peaks. This is because the number of primary collisions is larger for the longer pads, and the width of the peak therefore narrower, according to the Poisson distribution in Eq. 5.

With a 2 parameter scaling it is in general possible to give a good description of the region around the peak. The scaling suggested by Bichsel it to align the $\Delta_l$ and the $\Delta_u$ (see Figure 2). This scaling can be understood quite intuitive since $P(E)$ does not depend a lot on $\beta\gamma$ for relevant small energy losses, so the main difference between straggling functions

6

for different $\beta\gamma$ is the number of collisions $\mu$ (the total energy loss $\Delta$ is roughly proportional to $\mu$ while the width is roughly proportional to $\sqrt{\mu}$).

It is important to understand the scaling of straggling functions when the truncated mean is constructed from cluster charge measurements of $Q$ with different pad geometries (such as in ALICE). Figure 4 shows that a naive normalization to the track length will not work and that an alignment of the different straggling functions is non-trivial. However, we are often saved by the fact that tracks have similar structure so that we bias them in the same way [2].

The two parameter scaling is also useful for straggling functions for particles with different $\beta\gamma$ and we shall study this in section 3.1.

# 3    Reanalysis of the energy resolution

The test beam data were collected using an ALICE IROC with 63 pad rows and a pad size of 4 mm $\times$ 7.5 mm. The tracks were going through the field cage parallel to the pad plane and perpendicular to the pad rows at a distance of $\sim 90$ cm. In the following $Q$ will be used to designate the total charge of a cluster, $Q_x$ for individual cell (pad-time bin) charges, $Q = \sum Q_x$, and the maximum cell charge $Q_{\mathrm{MAX}} = \mathrm{Max}(Q_x)$.

The first analysis of the test beam data is described in [7]. There the focus was on the truncated mean which is not very sensitive to the underlying physics. For this study it was therefore decided to refine the analysis:

- ALTRO treatment. Apply the tail cancellation and baseline correction filters as will be done in the final setup, see e.g. [10].

- Lower $Q_{\mathrm{MAX}}$ cut to 5 ADC ch. To keep the low energy clusters.

- Correct for cluster charge loss by the clustering algorithm.

- Correction for gain variation

The two runs used for this analysis were taken within 90 minutes. In this time interval the air temperature in the hall increased by 0.8 degrees, while all other temperatures (e.g. end-plate) increased by less, and the pressure dropped by 0.4 mbar. No corrections have been made for these variations. The density variation is less than 0.5%, but the gain variation might be a lot bigger (factor 5 [11]) since the Townsend amplification coefficient depends strongly on the density.

The application of the ALTRO filter was quite trivial since the ALTRO coefficients had already been extracted from the test beam data by Bernardo Mota and a software package simulating the ALTRO processing implemented by Roland Bramm existed.

The lowering of the $Q_{\mathrm{MAX}}$ threshold required a more careful selection of tracks since a few noisy neighboring pads easily generate many small noise clusters.

---

[2]An extreme case was the test beam data where a 40 % gain variation over the chamber lead to no decrease in energy resolution because all tracks had hits in almost all rows.
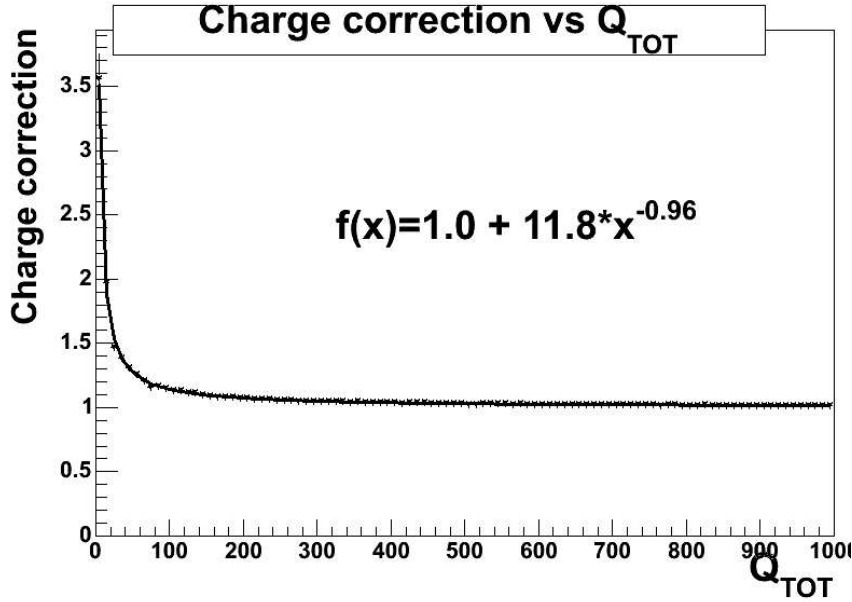
Figure 5: The correction for the cluster charge loss due to the threshold cut. $Q_{\mathrm{TOT}}$ is the total measured charge.

In the clustering algorithm only signals $Q_x$ of 3 ADC ch or more are used as input. This removes part of the tails from the clusters which can be a big effect for small charge clusters. To estimate this correction a simulation was developed with the following procedure:

- Only 1 pad row was studied

- Electrons were transported from the particle track height of 90 cm down to the pad plane taking into account transverse and longitudinal diffusion (but no transverse diffusion between rows)

- Exponential amplification was assumed for each electron (see also [2] section 4.6). The total expected charge in a pad row was calculated by summing up the charge after amplification.

- The charge was distributed in pad and time according to a Gaussian pad response function with width 2 mm and a gamma-4 shaping function with $\tau = 200$ ns.

- After all charge had been distributed, the charge was discretized and a threshold cut of 3 ADC was applied for each cell in the cluster. The summed charge above threshold yielded the measured charge.

The gain was in the simulation was adjusted using data (3 GeV/$c$ protons row 11-20) assuming that 17 electrons corresponded to the most likely peak, but the correction is not very sensitive to this. The calculations are more sensitive to the cluster shape which is dominated by diffusion (since the pad response/shaping functions are known). Comparing

8

data and simulation it was made sure that the cluster shapes agreed. The correction can be seen in Figure 5. It is large for small clusters, but these are also rare (in the 3 GeV/$c$ proton ($\sim$ MIP) setting 8.2% of the clusters had ADC $\leq$ 100). When the correction is applied to the data, the resulting straggling function becomes narrower.
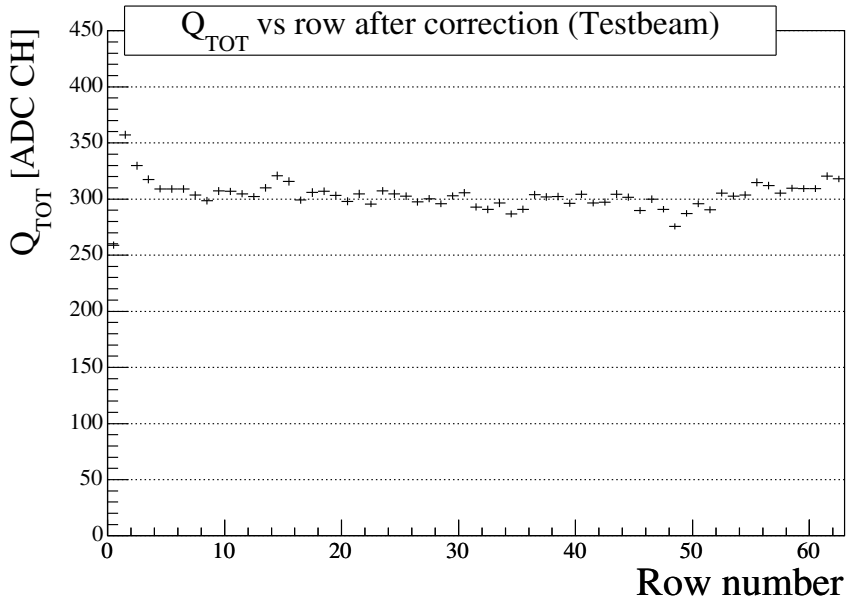


Figure 6: The mean total charge $\langle Q \rangle$ vs row after correction. When the first 3 rows are discarded the remaining rows shows only small variations (RMS = 2.8%).

The observed gain variations with the row number were fitted with a first degree polynomial and this was used to correct the data. The final correction is:

$$Q_{\text{corrected}} = \frac{1.0 + 11.8 \cdot Q_{\text{measured}}^{-0.96}}{1.0 + 0.422 \cdot \text{row}/62} \tag{6}$$

When charge is mentioned in the following it will always refer to the corrected charge unless otherwise mentioned.

The average charge per pad row as a function of row is shown in Figure 6. The fluctuations are small (RMS = 2.8%) when the first 3 rows are disregarded (as has been done in the following).
Finally the straggling function calculated from row 11-20 is compared with the one calculated from row 41-50 using the same set of data. As can be seen in Figure 7 the two curves are similar suggesting that the corrections are complete.
The measured straggling functions are shown in Figure 8 together with the truncated mean distribution. To extract the most likely energy loss ($\Delta_p$) and the FWHM ($w$) the histogram is fitted with a 5th order polynomial around the peak.
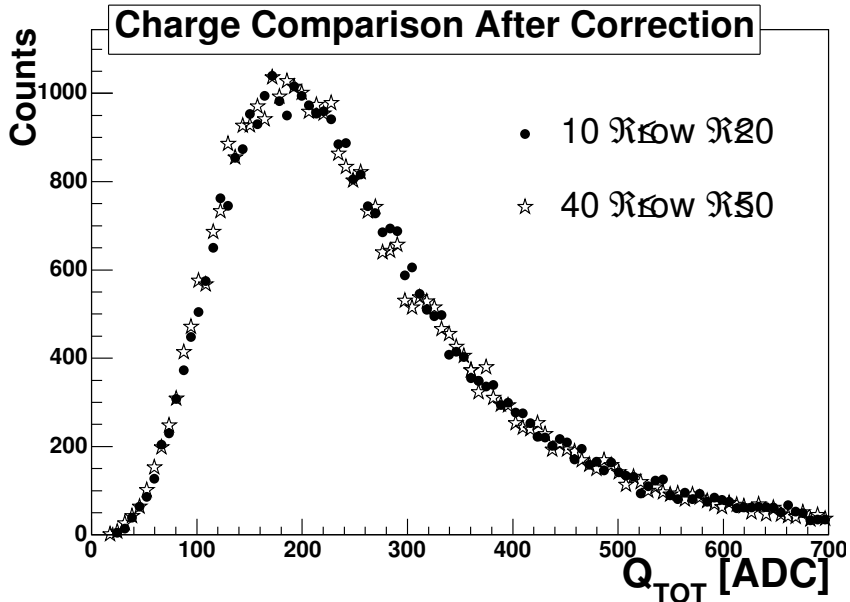
Figure 7: Comparison of the cluster charge distribution in row 11-20 with that in row 41-50 after all corrections.

It is important to realize that the Bethe-Bloch $dE/dx$ is different from $C$ and $\Delta_p$ as it gives the *average* energy loss which is dominated by the tail and not the peak. Therefore the truncated mean is here denoted $C$ as suggested by Hans Bichsel.

Figure 9 shows the comparison of the two straggling functions. The tails have similar shape and can be described by a power law ($\propto x^{-\alpha}$). Fitting the tails yields $\alpha = 3.40 \pm 0.04$ ($p = 1$) and $3.20 \pm 0.04$ ($p = 3$)

## 3.1 Experimental scaling of the straggling functions

In the last section the scaling of straggling functions was discussed. From Bichsel's calculations it is found that to scale the 3 GeV/$c$ data to the 1 GeV/$c$ data the following two parameter scaling should be used:

$$Q_1 = 1.31688 \cdot Q_3 + 40.0 \tag{7}$$

The offset of 40.0 was found by converting the 0.11772 keV offset in Bichsel's calculation to an ADC offset using the scaling factor from Figure 12 (340 ADC/keV).

From the experimental data themselves it is possible to derive a single parameter scaling:

$$Q_1 = \frac{\Delta_p(1)}{\Delta_p(3)} \cdot Q_3 = 1.5813 \cdot Q_3, \tag{8}$$

and a two parameter scaling (see section 2.1) :

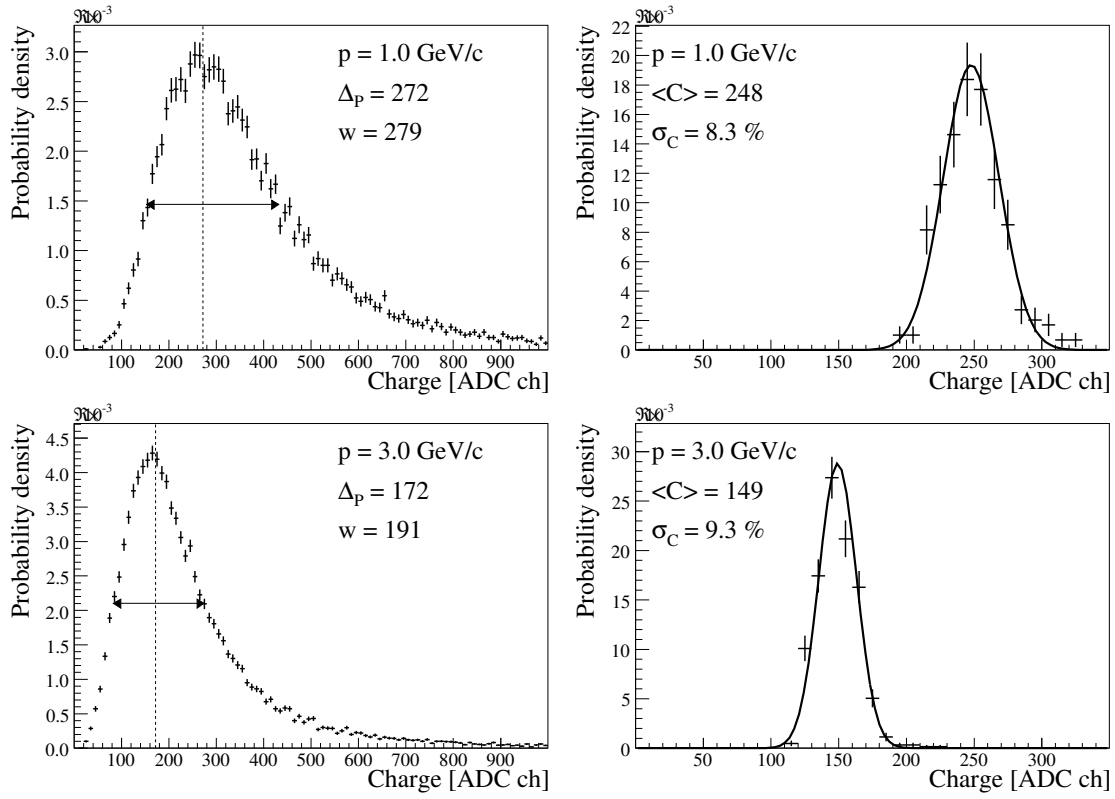$$Q_1 = 1.4609 \cdot Q_3 + 33.0. \tag{9}$$

10

Figure 8: Left: The measured straggling functions for segments. Right: The straggling functions for the truncated mean, $C$, for the tracks. The solid line is a Gaussian fit to the data. Both the measured distributions and the fit have been normalized to have integral 1.
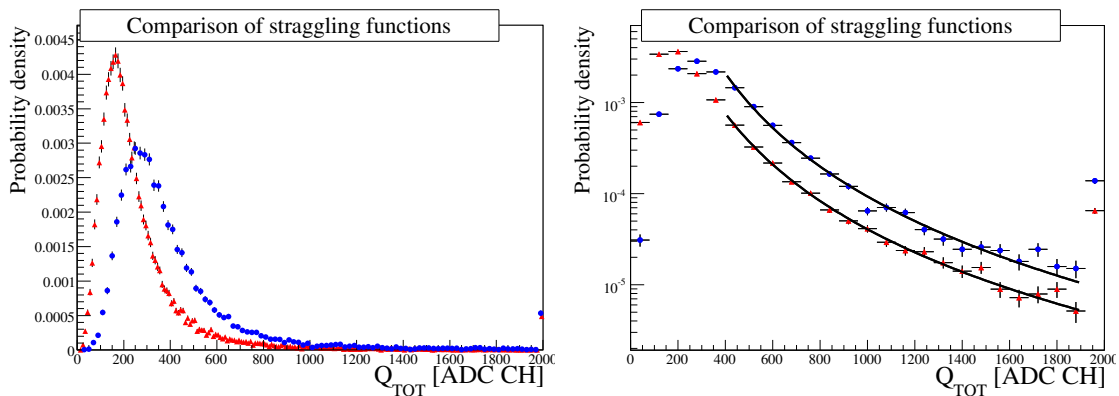


Figure 9: Comparison of the straggling functions for protons of 1 GeV/$c$ (blue circles) and 3 GeV/$c$ (red triangles).
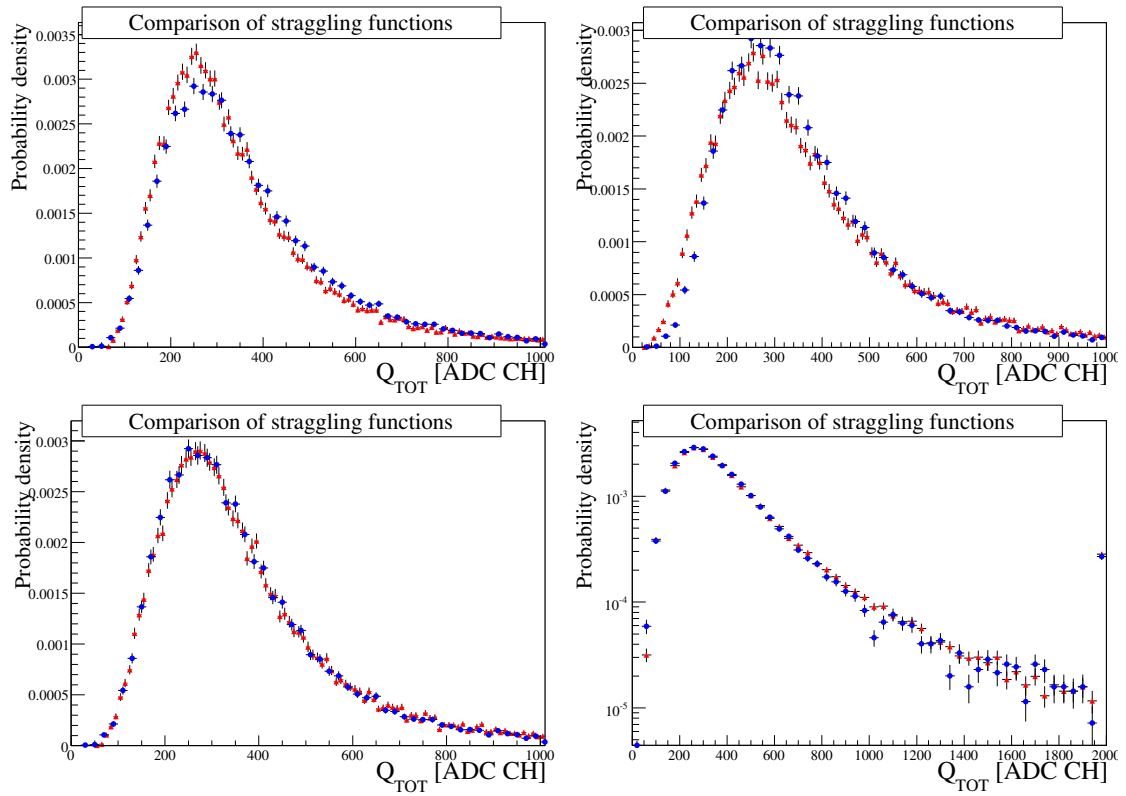
Figure 10: The figures all shows the $p = 3$ GeV/c after scaling (red triangles) compared to the $p = 1$ GeV/c (blue circles) one. Top left: Using Bichsel scaling (equation 7). Top right: Using single parameter scaling (equation 8). Bottom: Using two parameter scaling (equation 9), linear (left) and logarithmic (right).

Figure 10 shows the comparison of the scaled 3 GeV/$c$ straggling function to the actual 1 GeV/$c$ straggling function. The one parameter scaling fails to describe the structure around the peak, while the two parameter scaling based on the experimental data shows good agreement over the full range. The two parameter scaling from Hans Bichsel's calculations is slightly off, which is probably due to effects we shall see in the next section.

This however means that if one wants to use the scaling functions they must be derived from data or from calculations including all the corrections.

An important aspect of the two parameter scaling is that it is easy to construct a fit function from one good tabulated function. The scaling parameters can be optimized, and one can display the relevant parameters $\Delta_t$, $w$, and the normalization.
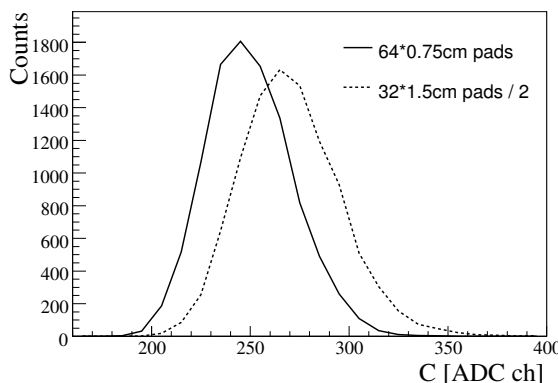


Figure 11: Comparison of the truncated mean distributions for 10,000 $p = 1$ GeV/c proton tracks for 64 short pads and 32 long pads with the naive scaling that the truncated mean for the long pads has been divided by 2. The peak of the distribution for the long pads is 8 % higher than for the short pads, while the relative width is 6 % less.

For completeness we show in Fig. 11 the naive comparison of the truncated mean from tracks of the same length but different pad length. This calculation is based on the simulation developed in the next sections. Clearly the naive scaling, $C_{\mathrm{long}} = 2 \times C_{\mathrm{short}}$, introduces large systematic errors. This shows another big difference between $dE/dx$ and $C$.

## 4 Comparison of data and calculations

For the model calculations a pure gas of Ne has been assumed. The density was taken to be the same as that of the of the Ne-$CO_2$-$N_2$ gas mixture at $T = 19$ °C, $p = 696$ mbar, $\rho = 0.910$ g/l (it would be 0.805 g/l for pure Ne). The difference is significant since the mean free path is inversely proportional to $\rho$.

The first comparison of data and calculation is shown in Figure 12. One parameter has been used to fix the conversion of eV to ADC (340ADC/keV), and both distributions have been normalized to have integral 1. The straggling functions are similar, but the energy
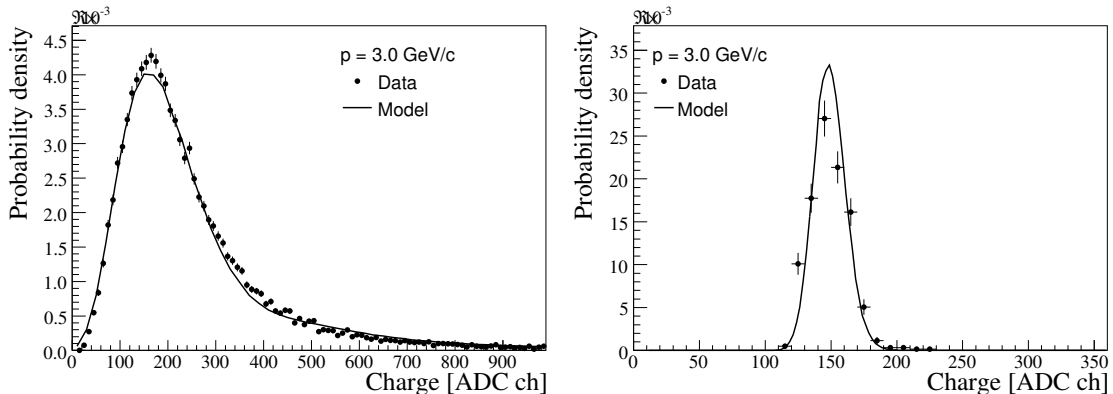
Figure 12: Comparison of the measured straggling functions and truncated mean distributions (data) to the model of Hans Bichsel (model).

resolution is different. In the simulation one finds $\sigma_E/E = 7.9\%$ ($p = 3$ GeV/$c$ , while the resolution of the data is $\sigma_E/E = 9.3\%$ (Figure 8).

To understand this discrepancy we first estimate the energy loss resolution from the experimental straggling function. The specific energy loss is calculated for 60 random cluster charges generated according to the straggling function histogram and the energy resolution is found to be 7.6%, which is simlar to the predictions from the model.
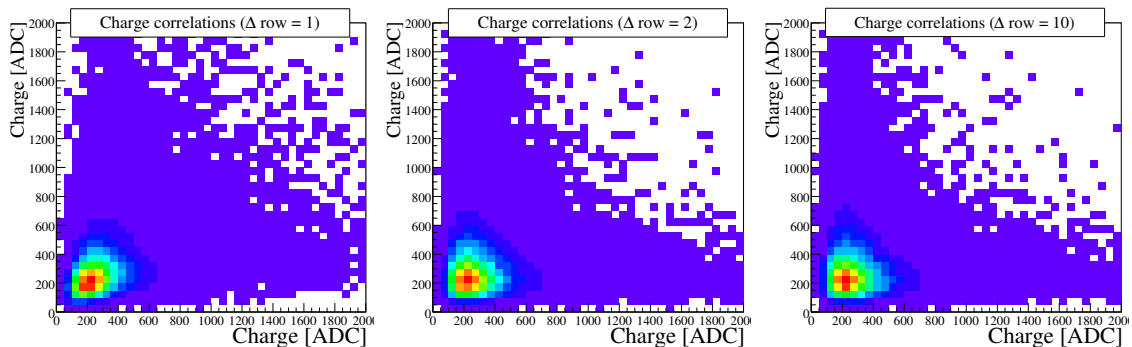


Figure 13: The correlation between charge measurements in different rows. Neighboring rows (left), 1 row in between (middle), and 9 rows in between (right).

This suggests that in a real track the ~60 charge measurements are not independent. Figure 13 shows the correlation between clusters in different rows. The correlation can be quantified with the correlation coefficient defined as:

$$\rho = \sum_i \frac{(x - \mu_x) \cdot (y - \mu_y)}{\sigma_x \sigma_y} \tag{10}$$

The correlation coefficient $\rho$ takes value between -1 (fully anti correlated) and 1 (fully correlated), while 0 means that the variables are uncorrelated (for this test), see e.g. [12].

The correlation coefficients for the data in Figure 13 are 0.33 (left), 0.02 (middle), and 0.0 (right), showing that adjacent rows are correlated. This correlation reduces the information contained in the 60 charge measurements.

The sources for correlations are:

- Diffusion. Transverse diffusion smears the deposited charge over a couple of rows.

- Anode-wire coupling between rows. The ions produced at the anode wire of one row couples capacitively to pads in the neighboring rows.

- Delta rays. High energy electrons will deposit their energy over multiple rows. This effect is very likely small.

The effect on tracking of the two first subjects have been studied by the STAR TPC group [13].

The theoretical (energy loss) and the experimental (cluster charge) straggling functions are quite different. To see if the observed effects could be explained and better agreement with the experimental straggling function reached it was decided to make a simple simulation. Only the diffusion and the amplification variation was taken into account.

The first problem was to convert the theoretical energy loss to ionization. Since the aim was to use the straggling functions and not the underlying cross sections (as done in [1]) it was decided to convert with the energy per ion pair $W = 30$ eV i.e. $N_{electrons} = \text{Int}(\Delta/W)$.
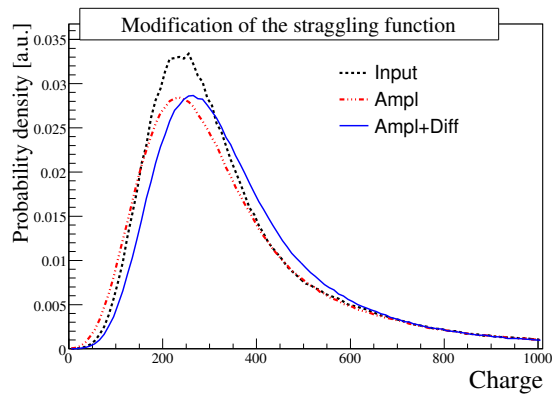


Figure 14: The modification of the straggling function calculated by Hans Bichsel as detector effects are taken into account.

The simulation chain then looks like this where the curves refer to Figure 14:

- The TPC consists of 64 rows (2 outer + 60 central + 2 outer). Only the 60 central rows are used for comparison with the data. The outer rows are purely to simulate the charge flowing in and out at the edges.

- For each row an energy loss is generated from the Bichsel straggling function and converted to primary ionization by the energy per ion pair function. The "Input"

curve shows the number of primary electrons smeared out and multiplied by the average gain.

- An exponential amplification gain is randomly assigned to each electron ("Ampl" curve).

- Finally each electron is assigned a random position in the row and a random diffusion offset and the final row where the electron is amplified is calculated ("Ampl+diff" curve).

Figure 14 shows how the $p = 1$ GeV/c simulated straggling function is modifies when detector effects are taken into account. The tail is stable while the peak is broadened a bit.
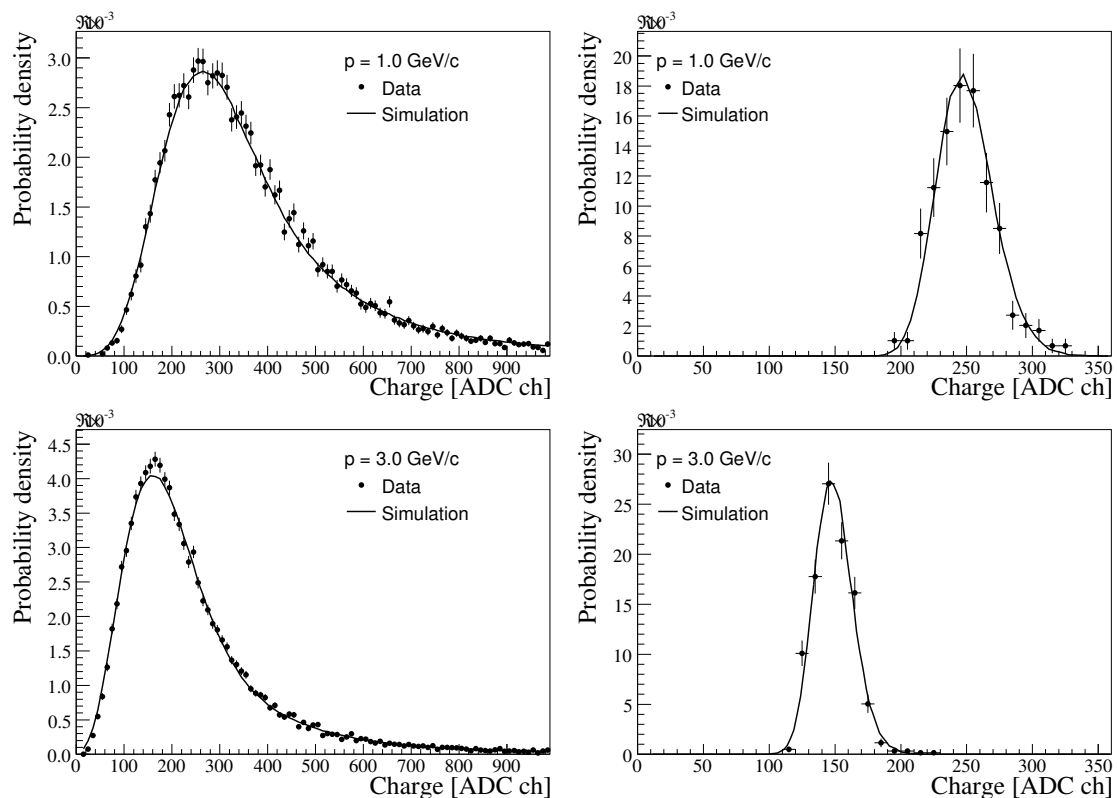


Figure 15: Comparison of the measured straggling functions and truncated mean distributions (experimental data) to the model of Hans Bichsel with detector effects included (simulation).

Figure 15 shows the comparison of simulation with the data. The agreement is now close for both the straggling functions and the truncated mean distributions indicating that the simulation has also introduced plausible correlations between cluster charges in track. We therefore conclude that it is possible to describe the measured straggling functions and

specific energy loss distribution with good precision from Bichsel's energy loss straggling functions when detector effects are taken into account. We further note that the resulting straggling function does *not* contain all information necessary to derive the energy resolution for the TPC i.e. the correlations between measurements in neighboring rows are important as they worsen the resolution and this information is not available in the straggling functions. This also suggests a fundamental problem with an approach based on fitting the cluster charges in a single track, since the fit will be biased.

# 5 Consequences for the final ALICE TPC

In this section, the simulation developed in the last section is used to study the resolution of the final ALICE TPC and the implications for PID. Since the extrapolation from 90 cm drift to 250 cm drift affects only the diffusion and the effect is small, the results should be quite precise.

The ALICE TPC readout chambers has 3 pad geometries (0.75, 1.0, and 1.5 cm pad length). The simulation is straightforward to extend for the 1.5 cm pads since here the energy loss is just the sum of 2 energy losses. In the following we shall therefore focus on these two pad geometries.
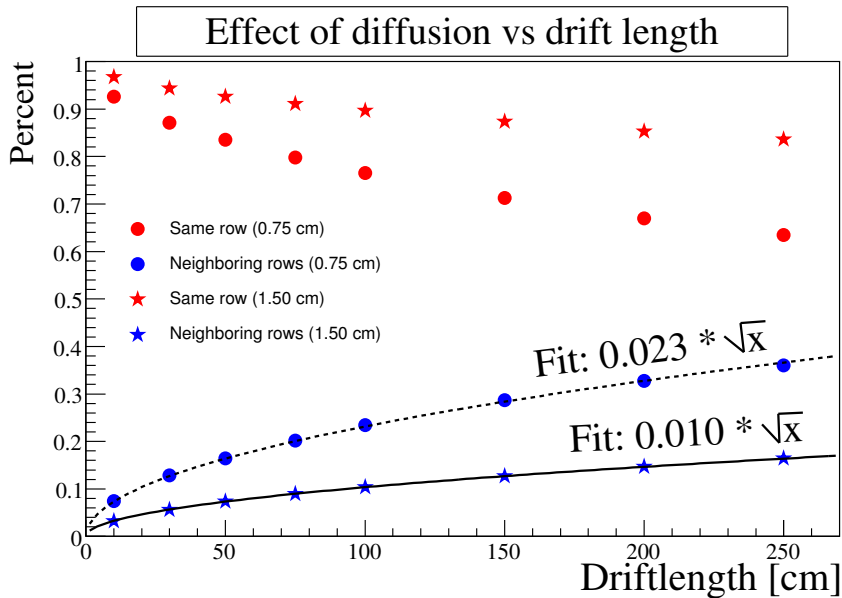


Figure 16: The sharing of charge produced over one row due to diffusion. The calculations were done for no magnetic field. The diffusion constant is $D_T = 220 \ \mu\text{m}/\sqrt{\text{cm}}$.

Figure 16 shows the signal sharing due to diffusion for the two pad geometries. The signal going to the neighboring rows is shared between the two neighbors. In a magnetic field the diffusion constants are decreased by a factor: $1 + (\omega\tau)^2$, $(\omega\tau = B \cdot v_{\text{drift}}/E)$. For full

17

magnetic field, $B = 0.5$ T, this factor is 1.13 which corresponds to an effective drift length reduction of $\sim 25\%$ compared to the case with no magnetic field.

| | Bichsel | 0 cm | 90 cm (nf) | 250 cm (nf) | 250 cm (ff) |
|---|---|---|---|---|---|
| $60 \times 0.75$ cm pads | 7.9 (139) | 9.0 (134) | 9.6 (153) | 9.8 (161) | 9.7 (159) |
| $30 \times 1.50$ cm pads | 8.4 (161) | 9.3 (158) | 9.7 (169) | 9.9 (174) | 9.8 (173) |

Table 1: The energy loss resolution for 3 GeV/$c$ protons for different cases: Bichsel, means without any detector effects and nf and ff, means no field and full field respectively. The mean of the truncated ADC value $< C >$ is given in the parentheses.

To compare the effect on the straggling function and the truncated mean we shall first compare 60 rows of 0.75 cm to 30 rows of 1.5 cm (cluster charge is divided by 2). Table 1 shows the value of the truncated mean and the resolution. The effect of going from 90 cm to the full 250 cm drift is small and almost compensated by the magnetic field. The basic resolution of the longer pads are less than that of the shorter, but when detector effects are taken into account the difference is small.

| Momentum | Total | Short (IROC) | Long ("OROC") |
|---|---|---|---|
| 1 GeV/c | 4.9 (177) | 7.4 (173) | 6.4 (177) |
| 3 GeV/c (MIP) | 4.4 (282) | 6.7 (277) | 5.8 (282) |

Table 2: The total energy loss resolution for full tracks in the ALICE TPC (250 cm drift and full magnetic field) and the contribution from the two readout chambers. The truncated mean value $C$ is given in the parenthesis's.

To study the effect on tracks in the full ALICE TPC we shall assume that it consists of $63 \times 0.75$ cm (IROC) $+ 75 \times 1.5$ cm (OROC) rows (The actual geometry is $63 \times 0.75$ cm $+ 64 \times 1.0$ cm $+ 32 \times 1.5$ cm). The straggling functions for the two pad sizes are different so the charge on the shorter pads were scaled as described in section 2.1 (for a MIP: $Q_{\text{scaled}} = 0.83924 \cdot Q + 42.7$).

The results from the simulation are shown in table 2. The resolution of the short pads are much better than shown in table 1, but that is an effect of the scaling e.g. for 3 GeV/$c$ protons we find $\sigma_{\text{effective}} = 7.4/(173.1 - 42.1) = 9.8\%$ which is similar to the values in table 1.

The truncated mean of the shorter pads is slightly less than that of the long pads even though the straggling functions have been scaled to be almost identical. This might be due to different correlations in the charge measurements.

The resolution for the full track is similar to what would be expected from the two chamber regions i.e. $\sigma_{\text{total}} \sim \sqrt{\sigma_{\text{short}}^2 + \sigma_{\text{long}}^2}/2$. This indicates that the adding of the two cluster samples have been done correctly.

The value of 4.9 % for a MIP particle is better than in the TDR (5.5%, [1] p.169) and the resolution will be the same or better for all other $\beta\gamma$. The value of 4.4 % for a 1 GeV/$c$ proton suggest that this is the best valuable achievable at higher $\beta\gamma$ e.g. for electrons.
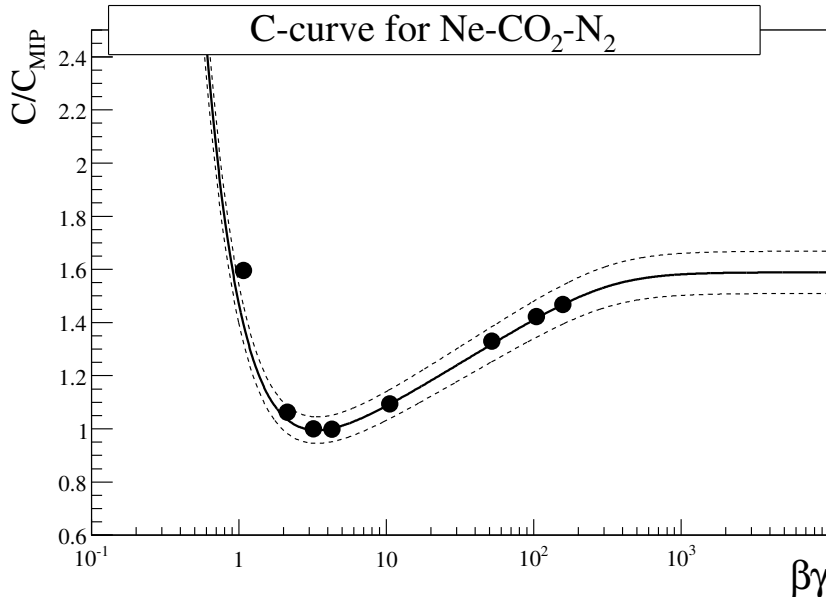


Figure 17: The dependence of the truncated mean, $C$, on $\beta\gamma$.

To estimate the PID separation power of ALICE TPC under these ideal conditions we shall assume that the energy resolution is 4.9 % for all $\beta\gamma$. The truncated mean as a function of $\beta\gamma$ can be estimated from the simulations and Figure 17 shows the comparison to the TDR ALEPH curve. As can be seen the agreement is reasonable and in the following the TDR curve has been used to estimate the separation power.

The separation power between pions and a particle specie, $X$, can be defined as:

$$D_X/\sigma = \frac{C_\pi - C_X}{\sigma} \qquad (11)$$

where $\sigma$ can either be $\sigma_\pi$ (Figure 18) or $\sigma = (\sigma_\pi + \sigma_X)/s$ (Figure 19). The latter gives a more realistic picture of the separation power.

Figure 18 shows the ALICE separation power compared to STAR. The comparison is not entirely fair as the STAR separation plot is based on actual central $Au + Au$ data where the performance of the ALICE TPC is worse ([1], page 169).

Figure 19 shows the separation in terms of the average resolution. The separation of pions and protons is $4\sigma$ for $3 \leq p_T \leq 20$ and the separation of pions and electrons is $4\sigma$ for $p_T \leq 6$. The kaons are close to protons in the full $p_T$ interval, but they can also identified from their decay products; in [4] it was shown how this contribution if known can be used to solve the proton-kaon ambiguity).
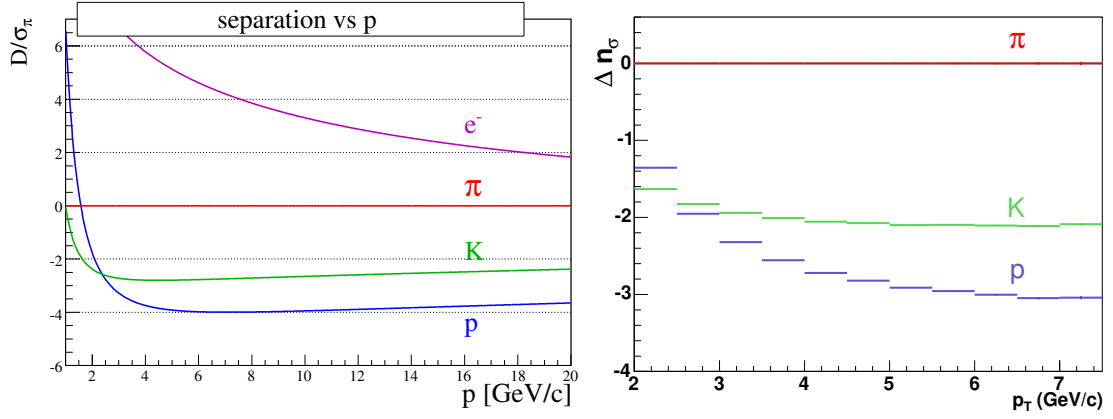
19

Figure 18: Comparison of the particle identification separation for ALICE and STAR. The STAR figure was taken from [4].
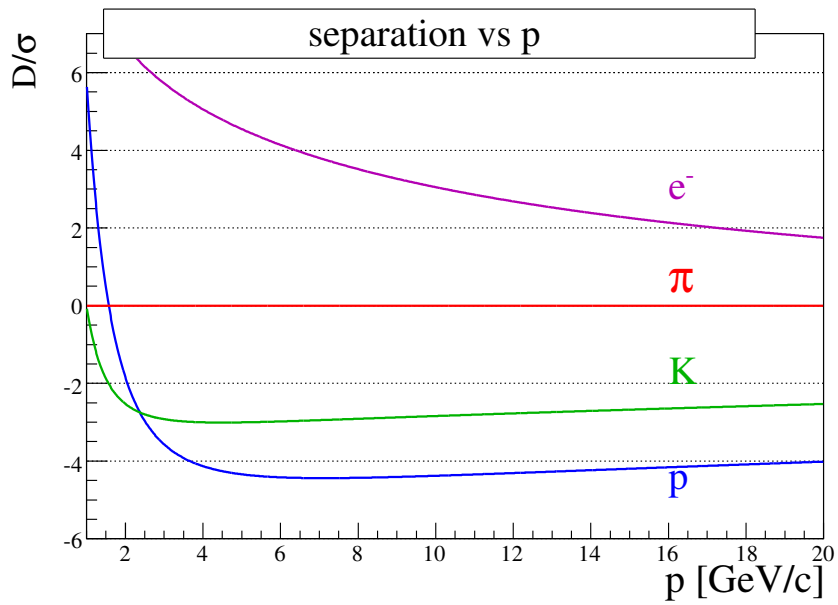


Figure 19: The particle identification separation for ALICE.

# 6  Conclusions

The energy loss resolution of the ALICE TPC has been studied using the test beam data, and has been found to fulfill the design requirements.

The model calculations of Hans Bichsel gives a precise description of the data when detector effects are included and should be part of the basis for a maximum information calibration and optimization of the detector and PID. The energy loss distribution (and correlation effects) also influences the space point resolution which depends on the number of ionization electrons.

Here is a few concrete suggestions for how one could proceed to optimize the PID with the final ALICE TPC.

- Use data from test beams or p+p collisions, where the track density is low, to calibrate and optimize the PID.

- Use truncated mean distributions for PID. All our studies indicates that it is not an advantage to fit the cluster charges in a single track since their values are correlated.

- Use a model (e.g. Bichsel's) that reproduces the data, as a help in optimizing the truncated mean method. As can be seen from Fig. 11 the normalization to the track length over the pad introduces systematic errors.

- Use the model/simulation to constrain as much as possible the PID fits. Use the data where other detectors, such as RICH or TOF, can fully discriminate particles to validate this approach.

The results presented here indicate that particle identification can be achieved even at intermediate and high transverse momentum. The studies of simpler systems will help to improve the study of high multiplicity Au+Au events and allow many interesting physics quantities to be extracted.

# References

[1] Alice Collaboration, "Time Projection Chamber", ALICE TDR.

[2] W. Blum and L. Rolandi, "Particle Detection with Drift Chambers", Springer-Verlag ISBN 3-540-56425-X. .

[3] F. . (. Carminati *et al.* [ALICE Collaboration], J. Phys. G **30**, 1517 (2004).

[4] O. Barannikova, "High transverse momentum identified particle spectra in 200-GeV collisions from STAR", arXiv:nucl-ex/0505021.

[5] O. Barannikova, Talk at Quark Matter 2005.

[6] M. Shao, O. Barannikova, X. Dong, Y. Fisyak, L. Ruan, P. Sorensen and Z. Xu, "Extensive particle identification with TPC and TOF at the STAR experiment", arXiv:nucl-ex/0505026.

[7] P. Christiansen et al for the Alice TPC Collaboration, "Performance Test of the ALICE TPC IROC Module at the PS", ALICE-INT-2005-029.

[8] H. Bichsel, "A method to improve particle identification in TPCs and silicon detectors", to be submitted to Nucl. Instrum. Meth. A,
also see the website `http://faculty.washington.edu/hbichsel`.

[9] H. Bichsel, "Straggling In Thin Silicon Detectors", Rev. Mod. Phys. **60**, 663 (1988).

[10] R. Bramm, Ph. D. thesis, Johann Wolfgang von Goethe - Universität in Frankfurt am Main (2005), [arXiv:physics/0501052].

[11] M. Hauschild *et al.*, Nucl. Instrum. Meth. A **314**, 74 (1992).

[12] G. Cowan, "Statistical Data Analysis", Oxford University Press, ISBN: 0198501552

[13] STAR TPC web page (hardware/signal and couplings),
`http://www.star.bnl.gov/STAR/html/tpc_l/tpc.html`